Heliyon 8 (2022) e10504

Contents lists available at ScienceDirect

Heliyon

journal homepage: www.cell.com/heliyon

Research article

Modulation of the carrier balance of lead-halide perovskite nanocrystals by polyelectrolyte hole transport layers for near-infrared light-emitting diodes

Chih-Chien Lee [a], Johan Iskandar [a,c], Ade Kurniawan [a,c], Hung-Pin Hsu [b,c], Ya-Fen Wu [b,c], Hsin-Ming Cheng [b,c,*], Shun-Wei Liu [b,c,**]

[a] Department of Electronic Engineering National Taiwan University of Science and Technology, Taipei City 106335, Taiwan
[b] Department of Electronic Engineering, Ming Chi University of Technology, New Taipei City 243303, Taiwan
[c] Organic Electronics Research Center, Ming Chi University of Technology, New Taipei City 243303, Taiwan

ARTICLE INFO

Keywords:
NIR PeLEDs
Charge balance
P3CT
Hole transport layer

ABSTRACT

An alternative material, methylamine (MA)-doped poly[3-(4-carboxymethyl)thiophene-2,5-diyl] (P3CT) as hole transport layer (HTL) was investigated for efficient solution-processed near-infrared perovskite light-emitting diodes (NIR PeLEDs). The best NIR PeLEDs performance was achieved with an optimized composition ratio of the MA-doped P3CT (1:1) due to the balance of the electron and hole carrier in the active layer. The charge-balanced NIR PeLEDs exhibit the highest radiance of 858.37 W sr^{-1} m^{-2}, a low turn-on voltage of 1.82 V, and an external quantum efficiency of 7.44%. Our findings show that using P3CT as an alternative HTL has the potential to significantly improve PeLED performance, allowing it to play a role in the development of practical applications in high-power NIR LEDs.

1. Introduction

Metal halide perovskites have unique properties such as bandgap tunability, balanced carrier mobility, and low exciton binding energy, which make them suitable for use in optoelectronic devices [1, 2, 3]. In recent years, intensive research on modifying the perovskite precursor solutions, film morphology, and interface engineering has increased perovskite solar cell efficiency up to 25% [4, 5]. Together with their superior photovoltaic performance, hybrid perovskites exhibit strong photoluminescence (PL) properties with high color purity, making them desirable candidates for the low-cost light-emitting diodes (LEDs) [6, 7, 8]. To date, various approaches to improving perovskite LEDs (PeLEDs) performance have been investigated, including designing novel device structures, optimizing the structure of perovskite and charge transport materials, and lowering injection barriers between charge transport layers and perovskite layers [9, 10, 11, 12, 13, 14].

The crystallinity of the perovskite emissive layer is an important factor in the performance of PeLEDs [15, 16, 17, 18]. The layer on which the perovskite emissive layer is grown has a substantial impact on the perovskite's crystal characteristics such as grain size and morphological defects. These characteristics are critical for manufacturing high-efficiency perovskite light-emitting diodes. Smaller perovskite grains are anticipated to shorten carrier diffusion, which is advantageous in perovskite LED applications [19, 20, 21, 22, 23]. A crystal structure with small grains can also provide appropriate surface coverage, decreasing pinholes and charge traps and therefore increasing carrier recombination [15, 24]. To reap all of these benefits, the underlayer (i.e. p-type HTLs for p-i-n PeLEDs architecture) must be optimized as a site for perovskite layer growth.

Typically, most p-i-n PeLEDs utilize poly(3,4-ethylenedioxythiophene) polystyrene sulfonate (PEDOT:PSS), poly(9,9-dioctylfluorene-alt-N-(4-sec-butylphenyl)-diphenylamine) (TFB), poly(9-vinylcarbazole) (PVK), and poly(N,N′-bis-4-butylphenyl-N,N′-biphenyl)benzidine (Poly-TPD) as HTLs [11, 13, 25, 26]. Due to their low-temperature solution processability and good wettability, conjugated polyelectrolytes composed of π-delocalized backbones and charged side groups appear to be a good choice for other HTL candidates. It has been reported that doped poly[3-(4-carboxybutyl) thiophene-2,5-diyl] (P3CT), such as P3CT-Na and P3CT-CH_3NH_2 (P3CT-MA) polyelectrolytes can be used for inverted highly efficient perovskite solar cells [27, 28].

In this paper, we investigate in depth a new candidate HTL material for PeLEDs, MA-doped P3CT, inspired by the desirable formation

* Corresponding author.
** Corresponding author.
E-mail addresses: SMCheng@mail.mcut.edu.tw (H.-M. Cheng), swliu@mail.mcut.edu.tw (S. Liu).

https://doi.org/10.1016/j.heliyon.2022.e10504
Received 1 June 2022; Received in revised form 26 August 2022; Accepted 26 August 2022

mechanism. Hole transport capability is modulated and enhanced, resulting in an improved balance of charge carrier transfer in the devices. The perovskite film on optimized HTLs had a smoother surface and better crystallinity with fewer defects, reducing non-radiative recombination and increasing device brightness. The radiance and external quantum efficiency (EQE) both increased to 858.37 W sr^{-1} m^{-2} and 7.44%. It has been proved that the proper perovskite material and/or charge-transporting materials are required for the development of high-performance PeLEDs. The mechanism of device performance improvement will be discussed.

2. Materials and methods

2.1. Materials

Methylammonium iodide (MAI, 99.99%) was bought from STAREK scientific Co., Ltd. Lead iodide (PbI_2, 99.99%) was bought from Alfa aesar. poly[3-(4-carboxylbutyl)thiophene (P3CT) was purchased from Rieke Metals. 3′,3‴,3‴ ˝-(1,3,5-triazine-2,4,6-triyl) tris(([1,1′-biphenyl]-3-carbonitrile (CN-T2T)) was bought from Shine Material Technology Co., Ltd. Methylamine (CH_3NH_2) solution 40 wt.% in H_2O, N-Butylammonium iodide (BAI), Chlorobenzene (CB), *N*,*N*-dimethylformamide (DMF), and Dimethyl sulfoxide (DMSO) were purchased from Sigma-Aldrich. All the chemical materials were directly used without any further purifications.

2.2. Precursor solution fabrication

The perovskite precursor solution (0.5 M) was made by dissolving PbI_2:MAI:BAI (1:1:0.2) in 1 mL of the mixed solvent (DMF:DMSO = 4:1 in volume) and stirring it for 12 h at room temperature in a N_2-filled glovebox. P3CT-MA was created by stirring P3CT with CH_3NH_2 (MA, molar ratios of 1:0.5, 1:1, 1:2, and 1:3) in methanol at 40 °C.

2.3. Device fabrication

The ITO-coated glass substrates were cleaned using detergent, deionized water, acetone, and isopropyl alcohol, which were then dried under nitrogen flow. The substrates were then exposed to UV-ozone for 20 min P3CT-MA with varying MA ratios was spin-coated on the ITO substrate for 60 s at 4000 rpm then annealed at temperature of 140 °C for 20 min. The substrates were transferred into a glove box filled with N_2 for perovskite deposition. Perovskite films were deposited in 30 s using an anti-solvent method at 5000 rpm. At 10 s after the spin coating began, 200 μL CB was added onto the substrate. Then the substrate was put on a hotplate at 90 °C for 10 min to form perovskite films. Following that, Liq (1 nm), CN-T2T (60 nm), Liq (1.2 nm), and an Al (100 nm) anode were thermally evaporated under a high vacuum (2×10^{-6} Torr). The devices' active area was 4 mm^2.

2.4. Characterization and measurement of devices

The Otsuka ELSZ-2000 series was used to perform dynamic light scattering (DLS) measurements. A JASCO V-770 UV-visible spectrophotometer was used to measure UV–Vis absorption. Surface roughness measurements were taken with a Bruker Innova AFM, and scanning electron microscopy images were captured with a JEOL JSM-7610FPlus Field Emission Scanning Electron Microscope. A Bruker D8 Advance diffractometer with Cu–K radiation was used for X-ray diffraction. A HORIBA FluoroMax Plus was used to collect steady-state PL and time-resolved photoluminescence (TRPL) spectra. The PL decay curves were measured using a HORIBA N-320 NanoLED pulsed diode controller at an excitation wavelength of 320 nm and a pulse frequency of 50 kHz. Temperature dependent emission spectra (from 10 K to 290 K) were recorded with a home-built setup. For cooling, the sample was put into a continuous liquid helium flow cryostat (Eyela, CA-2600) with excited by a HeCd laser (KIMMON KOHA, IK3252R-E) with 32n nm. The laser output power was achieved by combination of neutral density filters, which resulted in available fluences bellow 50 μJ cm^{-2}. After encapsulation with epoxy glue and a glass cover, the NIR PeLEDs were characterized. The EL spectra and J-V characteristics were obtained by using an Keysight Technologies B2901A connected with EnliTech LQ-100R. The C–V characteristics were measured under dark conditions using an XM Solartron at a fixed frequency of 1 kHz and a voltage range of 0–4 V. Hole-only devices were fabricated to measure the hole mobility of the MA-doped P3CT through the space charge limited current (SCLC) method. The mobility was calculated by fitting the dark current to a single carrier SCLC model.

3. Results and discussions

P3CT-MA was synthesized by reacting P3CT with the organic compound CH_3NH_2 (methylamine = MA). Figure 1a depicts the chemical structure of P3CT-MA. Methylamine was added to the P3CT solution in the following molar ratios: 1:0.5, 1:1, 1:2, and 1:3. For convenience, the P3CT-MA HTLs studied in this work are abbreviated as 0.5MA (Methylamine with a molar ratio of 1:0.5), 1MA (Methylamine with a molar ratio of 1:1), 2MA (Methylamine with a molar ratio of 1:2), and 3MA (Methylamine with a molar ratio of 1:3). Because P3CT cannot dissolve in the used solvent without the addition of MA, 0.5MA was designated as the control solution. The use of variable molar ratios of MA in the P3CT-MA solution resulted in significant changes in the size distribution of particle dispersions. The size distribution of synthesized P3CT-MA as a function of MA amount was investigated using dynamic light scattering (DLS). Figure 1b depicts the particle size distribution as a single peak (each solution is filtered with a 0.45 μm pore syringe filter made of hydrophilic polyvinyl difluoride (PVDF)). DLS measurements show that increasing the molar ratio of MA in the reaction mixture from the control solution to 3MA results in the formation of P3CT-MA with a decrease in particle mean size from around 342.6 nm–59.3 nm. The large mean particle size of control sample is most likely due to the P3CT not being completely dissolved in the solvent used. This is demonstrated by the control solution color, which remains black, just like the P3CT powder color (Supplementary Figure S1a). However, as the MA content increased, the solution color changed from black at control solution to orange and clear at 1MA, 2MA, and 3MA, indicating good solubility in the employed solvent.

Following the studies in solution, we investigated the optical properties of the deposited P3CT-MA thin films on ITO/glass substrates to determine the effect of different amounts of MA on the P3CT-MA HTLs. The transmittance gradually decreases as the MA content increases, as shown in Figure 1c. The decrease in transmittance as MA content increases is due to increased thickness from ~15 nm of control film to ~21, ~27, and ~35 nm of 1MA, 2MA, and 3MA, respectively (Supplementary Figure S1b). As is well known, transmittance is inversely proportional to absorbance. As the thickness of the film increases, more light is absorbed and transmittance decreases.

In general, employing hole transport materials with comparable energy levels and proper hole mobility can improve PeLEDs quantum efficiency [29]. P3CT-MA with different molar ratios of MA were used in our prepared NIR PeLEDs to investigate the influences of HTL on the device's performances. It is well understood that using various HTL can result in different electrical properties of the devices. A hole-only device (HOD) with the ITO/MoO_3/P3CT-MA/MoO_3/Al architecture was built, as shown in Figure 1d inset. The space charge limited current (SCLC) method is used to assess the hole mobility of P3CT-MA HTLs. As shown in Figure 1d, increasing the amount of MA significantly increased hole mobility (fitted line in supplementary Figure S2a). When compared to the device with control and 1MA, the HODs with 2MA and 3MA exhibit the highest current density at the same voltage, demonstrating the highest hole injection and transportation efficiency in the device. However, the hole mobility of the 1MA device matched well with the electron mobility

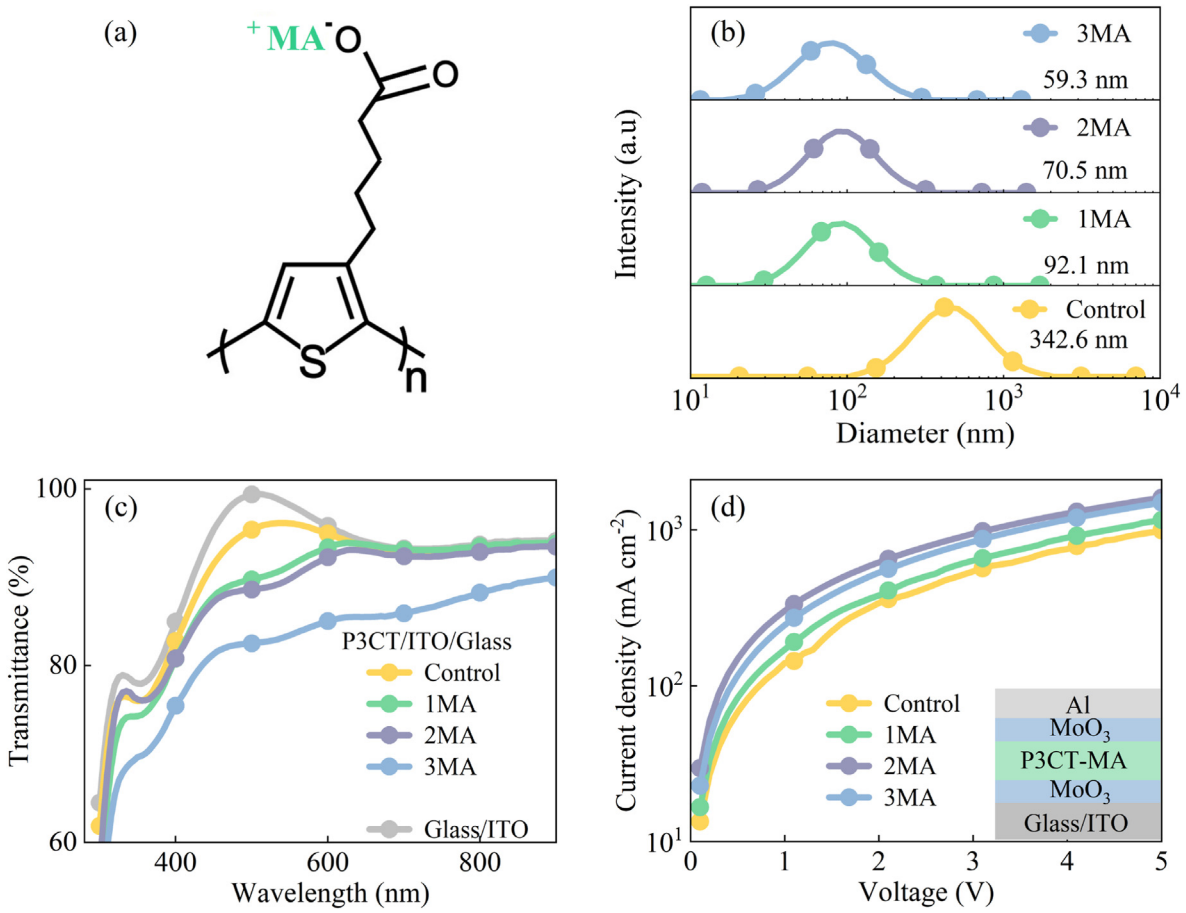

Figure 1. (a) Chemical structure of P3CT-MA, (b) Particle sizes of aggregated P3CT-MA in methanol solution with different MA contents, (c) Transmittance spectra of P3CT-MA films with different MA contents, (d) The voltage dependence of current density for the hole-only devices utilizing P3CT-MA HTLs with different MA contents.

of the electron-only device (supplementary Figure S2b and Table S1), resulting in the best device performance and a favorable balanced charge injection/transport in the NIR PeLEDs.

Atomic force microscopy (AFM) was used to determine the surface morphologies of control, 1MA, 2MA, and 3MA films. The root-mean-square (RMS) roughness values of the control, 1MA, 2MA, and 3MA films are 3.44 nm, 3.15 nm, 2.82 nm, and 2.46 nm, respectively, as shown in Figure 2a–d. The RMS of the P3CT-MA film is reduced by increasing the molar ratio of methylamine, indicating a smoother surface. A favorable morphology of HTL can improve hole transfer efficiency and reduce leakage current. Furthermore, the smooth surface of HTL may provide good contacts for upper perovskite.

Scanning electron microscopy (SEM) and atomic force microscopy (AFM) were also used to investigate the effect of different methylamine ratios in P3CT-MA layers on perovskite morphology. Top-view SEM images of perovskite films deposited on various P3CT-MA layers are shown in Figures 2e–h. Perovskite films deposited on P3CT-1MA HTL exhibit a more uniform surface morphology than those deposited on other MA molar ratios. The perovskite film on control film has lower surface coverage and larger pinholes, which could lead to short circuits. As the methylamine molar ratio increases to 1MA, SEM images show adequate surface coverage and densely packed grains with fewer pinholes. However, as the molar ratio was increased to 2MA and 3MA, pinholes appeared gradually. AFM images of the perovskite on the different P3CT-MA HTLs are shown in Supplementary Figure S3. The $MAPbI_3$ films become rougher as the MA amount increases, with RMS roughness values of 1.56, 2.45, 2.97, and 3.25 nm for perovskite deposited on control, 1MA, 2MA, and 3MA, respectively. The increase in roughness may be due to an increase in the number of perovskite nucleation sites, which leads to the formation of agglomerated perovskite grains, as seen in the SEM image. Figure 3a depicts the x-ray diffraction (XRD) patterns of perovskite films on various P3CT-MA HTLs. The prominent diffraction peaks (110) and (220) in Figure 3a increase with increasing MA. The trend demonstrates how methylamine concentration can have a direct effect on the preferential orientation of the perovskite crystal. When the amount of MA in the P3CT increases, the full width at half maximum (FWHM) of the most pronounced diffraction signal of the (110) plane decreases from 0.587° to 0.409°. The change in FWHM indicates that the perovskite grain size can be tuned by varying the MA/P3CT ratio (Supplementary Table S2). This behavior is attributed to increased chemical coordination of MA^+ and Pb^{2+} as MA concentration increases. As shown in Table S1, the large crystal sizes are grown with a large amount of MA, as seen in the SEM top-view images in Figure 2. We hypothesize that reorienting the crystal plane of perovskite while using the hole transport layer with the appropriate addition of MA can improve carrier transportability. The diffraction pattern, on the other hand, shows double peaks of (004) and (220) crystal planes (Figure 3b), indicating that the crystal grains inside the perovskite layer are relatively disordered.

The enhanced and controlled crystallization of the perovskite film can improve the quality of the perovskite film and reduce the density of defects, affecting the diffusion length of the charge carriers and the efficiency of charge transport [20, 30, 31]. Defects, as is well known, create trap sites for electron and hole recombination, negatively impacting device performance.

The effect of P3CT-MA HTLs with varying MA amounts on the photophysical performance of perovskite films was investigated using

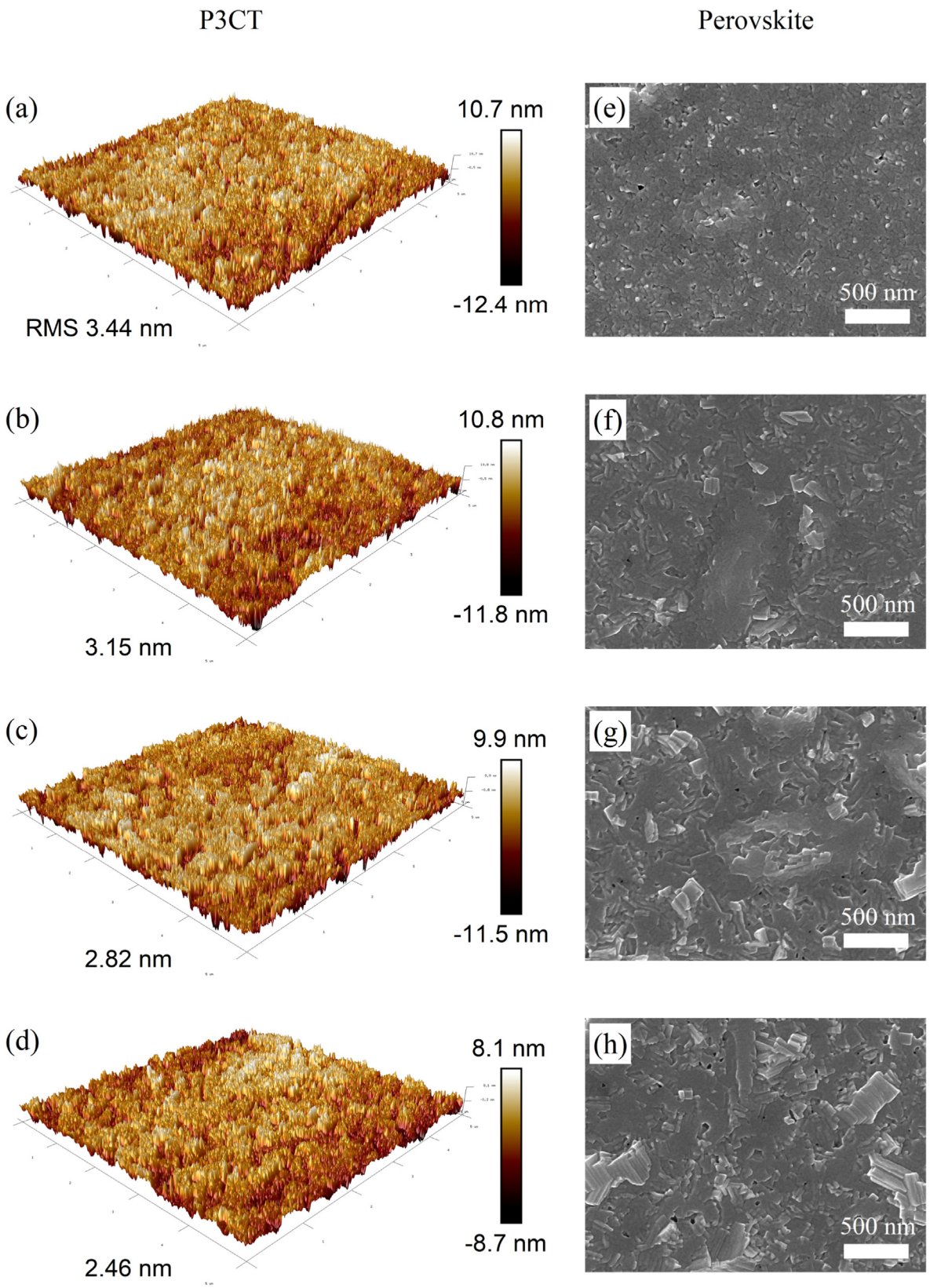

Figure 2. AFM images of P3CT-MA films grown with different molar ratios of (a) Control, (b) 1MA, (c) 2MA, (d) 3MA and SEM images of perovskite on P3CT-MA films with different MA contents of (e) Control, (f) 1MA, (g) 2MA, (h) 3MA.

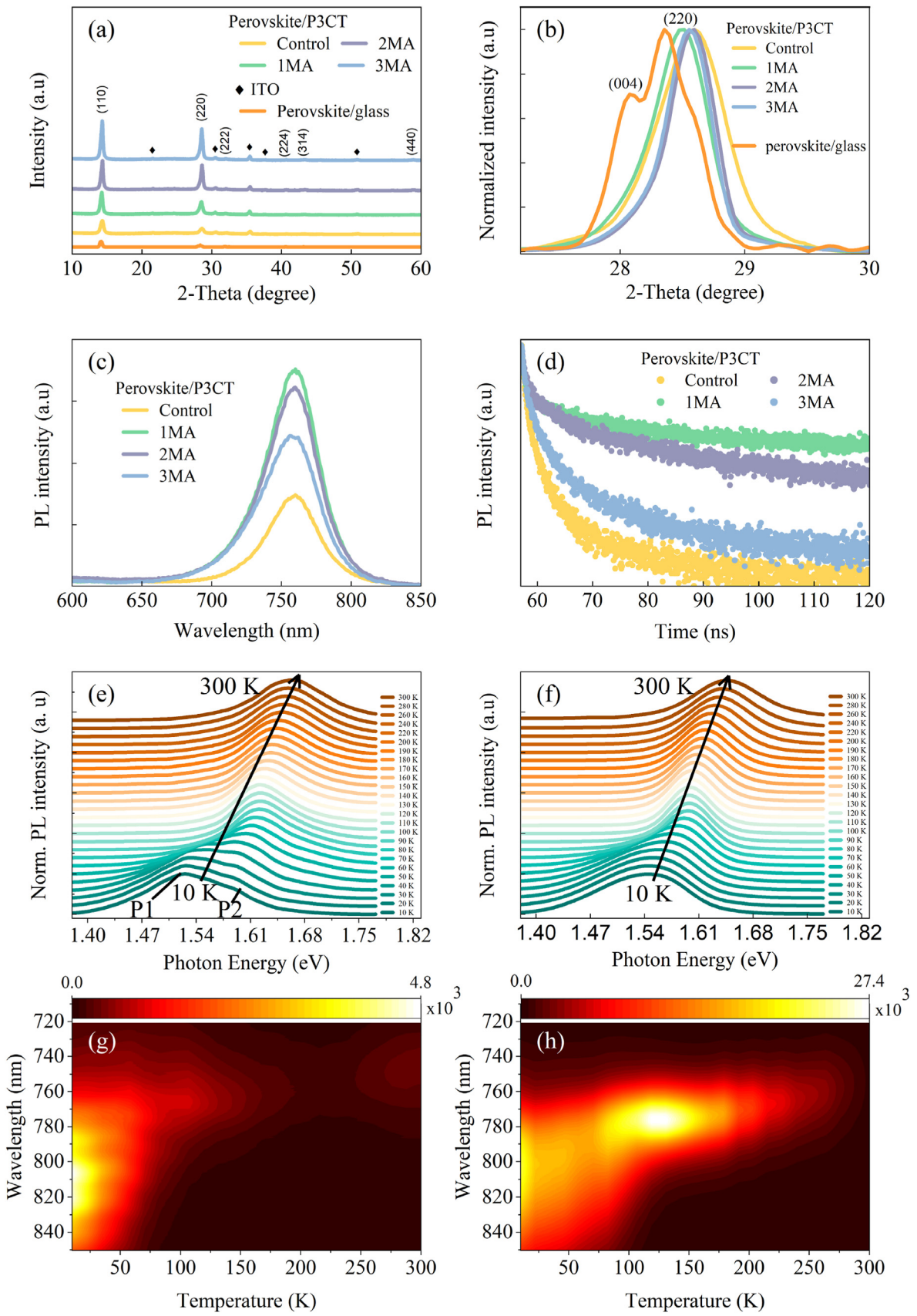

Figure 3. (a) XRD patterns of the perovskite film on glass and on the P3CT-MA films with different MA amounts, (b) enlarged XRD pattern of all perovskite film at (220) facet, (c) Photoluminescence spectra, (d) TRPL decay curve of the perovskite films covered on the P3CT-MA films with different MA contents, (e) and (f) Normalized temperature-dependent PL spectra of perovskite films on control and 1MA substrate, respectively, with a temperature ranging from 10 to 300 K, (g) and (h) Intensity of temperature-dependent PL spectra of the perovskite films on glass and on P3CT substrate, respectively.

steady-state and time-resolved PL (TRPL). Figure 3c shows that all samples have a similar PL emission peak around 759 nm, but the perovskite deposited on the 1MA has a much stronger PL intensity, indicating fewer traps and defects within the film. The increased PL intensity implies that non-radiative decay could be significantly suppressed, most likely due to increased crystallinity and decreased grain boundaries compared to the control film, which is consistent with SEM and XRD results [32, 33]. Meanwhile, due to the higher trap state density, the perovskite layer on the control substrate has lower PL intensity, resulting in higher trap-assisted recombination. Furthermore, TRPL decays were used to study the dynamics of exciton decay in perovskite films as shown in Figure 3d, which match bi-exponential expression (1) well [34].

$$I(t) = A_1 \exp\left(-\frac{t}{\tau_1}\right) + A_2 \exp\left(-\frac{t}{\tau_2}\right) \quad (1)$$

In which A_1 and A_2 are the decay amplitudes with lifetimes τ_1 and τ_2, respectively. The average lifetime (τ_{avg}) is calculated by using Eq. (2) [35]. The fitted values are shown in Supplementary Table S3. The average carrier lifetime for the control film is 13.74 ns, which is significantly improved by introducing MA. Perovskite film on 1MA has the longest average lifetime of 34.12 ns, indicating that the defect state density is reduced. However, when the molar ratio exceeds 2MA, the average lifetime decreases, which may be due to the emerging defect state caused by the rough perovskite film as shown in Supplementary Figure S3.

$$\tau_{avg} = \frac{\sum A_i \tau_i^2}{\sum A_i \tau_i} \quad (2)$$

We also investigate the effect of P3CT HTL on excitonic emission behavior by measuring the temperature-dependent PL spectra of two samples (the worst and the best PL intensity, as shown in Figure 3c), perovskite on control and 1MA films, as shown in Figure 3e,f. Figure 3e depicts the normalized spectra of perovskite films on the control substrate at various temperatures, with two peaks appearing in the low temperature sector (10 K) at around 1.52 eV and 1.58 eV. At 60 K, the low-energy peak (~1.52 eV) gradually fades, whereas the ~1.58 eV peak exhibits a continuous blueshift for its position. Furthermore, the peaks P1 and P2 correspond to orthorhombic and tetragonal phases [36, 37], respectively. For perovskite on 1MA, only one emission peak can be solved, indicating the absence of structural phase transition, and is also accompanied by a continuous blueshift of the emission peak, indicating increased bandgap with temperature increasing [38]. This is important because advanced optoelectronic device application requires stable perovskite structures over the operating temperatures. These blueshift phenomena are also happening to $CsPbI_3$ and $MAPbI_3$ as reported previously [38, 39]. This blueshift phenomenon is unusual and possibly related to thermal expansion and electron-phonon renormalization of the crystal lattice during heating [40]. As shown in Eq. (3), the Varshni empirical relation was used to interpret the temperature-dependent bandgap of semiconductors.

$$E_{gap} = E_{gap,\ 0K} - \frac{\alpha T^2}{\beta + T} \quad (3)$$

where α is the coefficient of change and β is the material's Debye temperature [41]. According to reference [42], the α for this type of perovskite has a negative value, and β is close to zero. As a result, as temperatures rise, the perovskite's PL peak exhibits a continuous blueshift. Furthermore, the exciton binding energy was calculated using the Arrhenius equation by plotting the integral PL intensity versus temperature (Eq. (4)).

$$I(T) = \frac{I_0}{1 + Ae^{\left(-\frac{E_b}{k_B T}\right)}} \quad (4)$$

in which I_0 is the emission intensity at 0 K, and A is the proportionality constant, k_B is the Boltzmann constant and E_b is the perovskite exciton binding energy. The fitted data are shown in Supplementary Figure S4. According to the fitting, the exciton binding energy for the perovskite on control and 1MA was 17.4 ± 1 meV and 38.6 ± 4.9 meV, respectively, which were close to previously reported values [43, 44, 45]. The relatively high E_b of $CH_3NH_3PbI_3$ ensures that excitons can survive above room temperature, which is beneficial for exciton-related optoelectronic application devices like LEDs and laser diodes.

Figure 3g,h show the temperature-dependent PL spectra plotted in 2D pseudo-color. The PL intensities of the perovskite films clearly show a tendency to decrease as temperature increases. This is most likely due to the additional thermal energy increasing the likelihood of the exciton dissociating according to a Boltzmann distribution [46]. Furthermore, the PL intensities of perovskite films on control substrate decrease sharply from 10 to 192 K and almost become undetectable above 200 K, whereas perovskite films on 1MA are detected very strongly from 10 K to 290 K, owing to their higher exciton binding energy. This result also implies that a perovskite film on 1MA has fewer surface trapping or thermally activated nonradiative recombination centers than a perovskite film on control sample [47].

A systematic ambient Raman spectroscopy characterization of perovskite thin films was performed to determine the time required to initiate the degradation process that is commonly observed in perovskite layers formed by the solution process when exposed to ambient conditions. Figure 4 depicts the evolution of Raman spectra caused by repeated measurements of perovskite layers deposited on various P3CT-MA HTLs with an acquisition time of 150 s for each spectrum. According to the spectra, $MAPbI_3$ decomposes to $CH_3NH_3^+$ and Pb–I in 330 s, as evidenced by bands at 94 cm^{-1} (Pb–I bond stretching mode) and 110 cm^{-1} ($CH_3NH_3^+$ bond liberation mode) [48, 49, 50]. Surprisingly, the band at 94 cm^{-1} becomes stronger within 330 s for perovskite films on control substrate (Figure 4a) and 3MA (Figure 4d) than for perovskite films on 1MA (Figure 4b) and 2MA (Figure 4c), implying that perovskite films on 1MA and 2MA are much more stable against degradation processes. Peak-to-peak ratios (p-t-p) between Pb–I and $CH_3NH_3^+$ bonds at 30 s and 330 s confirm this as well. Whereas the smaller p-t-p changes (Δp-t-p) suggest a slower degradation process (see supplementary Figure S5).

Utilizing the different optical characteristics of the above four perovskite films due to different HTL conditions, a NIR PeLEDs are constructed. Figure 5a depicts a schematic diagram of our NIR PeLEDs with the following layers: glass/ITO/P3CT-MA/perovskite/Liq/CN-T2T/Liq/Al, where P3CT-MA, perovskite, Liq/CN-T2T, take role as HTL, EML, and ETL, respectively, while ITO and Liq/Al are the electrode. To improve device's performance, we added a thin layer of Liq as a passivation layer between perovskites and CN-T2T, which is similar to a previously published paper with LiF [19, 25].

The EL spectra of NIR PeLEDs under 5.6 V driving voltage (Figure 5b) shows that the NIR PeLEDs with P3CT-1MA as HTL has higher luminance than the other three devices, indicating that at this condition, carrier transport is balanced and in favor of radiative recombination in the EML [51]. Figure 5c depicts the current density-voltage (*J*-V) and radiance-voltage (*L*-*V*) curves of NIR PeLEDs. According to the *J*-*V* curve, the NIR PeLEDs with control substrate demonstrated a higher current density and turn-on voltage when compared to the other three devices. The higher current density could be caused by the high density of surface defect trap states in the perovskite film deposited on control substrate, which corresponds to more pinholes. The photoluminescence properties of the perovskite emissive layer, as well as the energy and electric charge loss of LED devices, are greatly influenced by serving as a center of these defects for nonradiative decay [52, 53]. Because of the unbalanced mobility of holes and electrons in the control, 2MA, and 3MA-based devices discussed in the preceding section, recombination of electron-hole pairs does not occur in the middle of the active region,

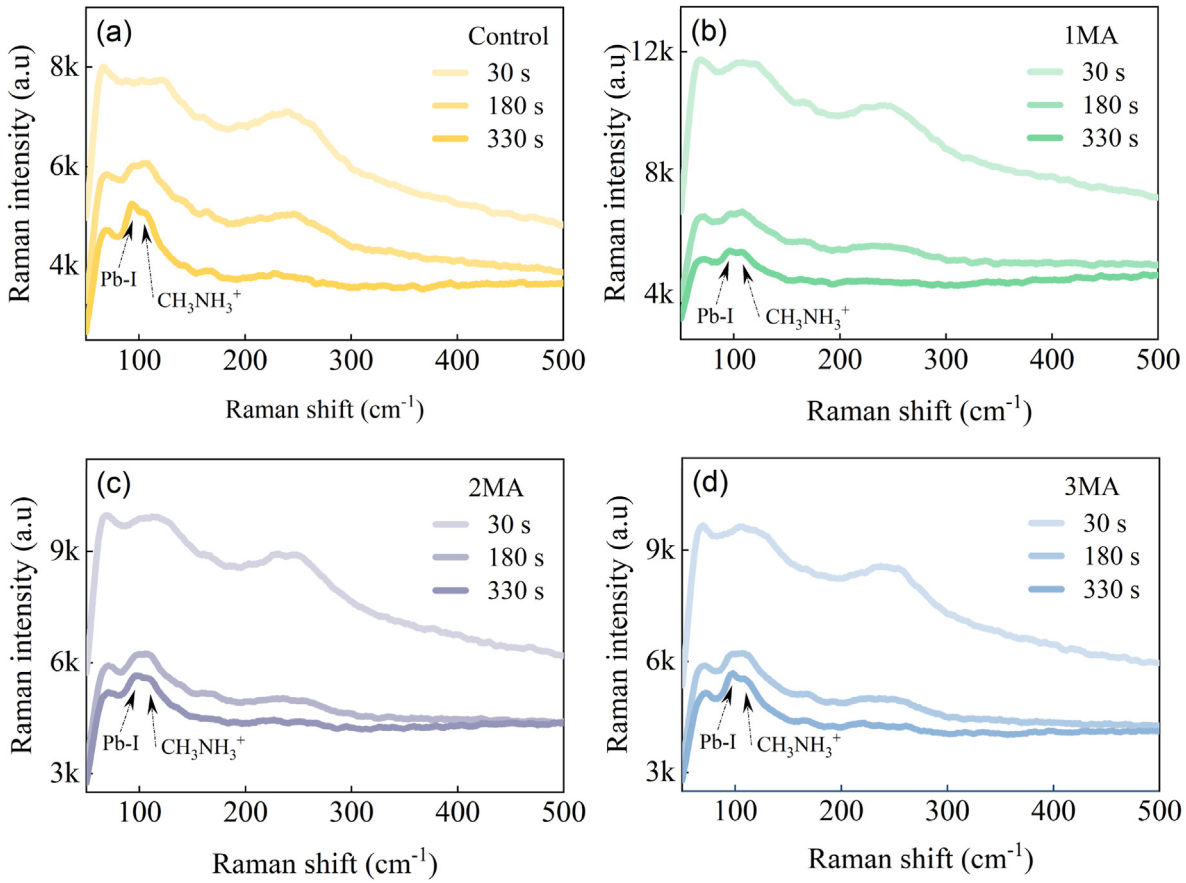

Figure 4. Time-dependent evolution of Raman scattering spectra from perovskite/P3CT-MA interface with different MA contents (a) Control, (b) 1MA, (c) 2MA and (d) 3MA.

resulting in reduced device performance, and thus the optimal device was achieved as the HTL was P3CT-1MA. Table 1 summarizes the performance of NIR PeLEDs with various P3CT-MA HTLs. The maximum radiance of the 1MA-based NIR PeLEDs is 858.37 W sr^{-1} m^{-2}, which is about a twelvefold improvement over the control device (71.38 W sr^{-1} m^{-2}). With high radiance, the *EQE* increased from 0.66% of the control device to 7.44% of the 1MA-based device, as shown in Figure 5d. Supplementary Figure S6 summarizes the peak EQE distribution for 48 devices with different P3CT-MA HTLs, demonstrating the repeatability of our device.

Capacitance-voltage (*C–V*) measurement was developed to further analyze the enhanced hole injection in the proposed NIR PeLEDs. It is possible to calculate the change in charge quantity in a NIR PeLEDs by measuring the differential capacitance using $dQ = CdV$. As a result, the *C–V* analysis is an efficient method for assessing carrier injection, transport, recombination, and charge balance in NIR PeLEDs [54, 55]. The *C–V* characteristics were measured in the dark at a fixed frequency of 1000 Hz Figure 6a depicts the *C–V* characteristics of NIR PeLEDs with various HTLs. The *C–V* plots show that the entire spectra can be divided into three regimes when dc-bias is applied. The flattest parts (first regime) are caused by depletion capacitance, which occurs when an externally applied voltage cannot suppress the built-in voltage (V_{built}) [19]. Because the voltage in this regime is less than 2 V, injected carriers in NIR PeLEDs are few, and *C–V* curves reflect device geometric capacitance. Because the capacitance value in this case is determined by the materials themselves, these two curves have nearly the same and unchanged value. We observed a continuous increase in capacitance at moderate applied voltages (second regime), indicating suppression of depletion regions due to charge injection and accumulation. The 1MA-based NIR PeLEDs, in particular, rises faster than the other three devices, which is most likely due to more and more carriers being injected in the device, and a higher number of injected carriers leads to a faster rise rate [56, 57, 58]. Because electron injection in NIR PeLEDs uses the same device structure Liq/CN-T2T/Liq/Al, the faster rise of the 1MA device curve can only be explained by enhanced hole injection that resulted in balanced charge injection into EML. The third regime is the decreasing part of capacitance in the *C–V* curve, which is caused by electron-hole recombination when the applied voltage exceeds the V_{built}. When the applied voltage is equal to and opposite to the V_{built} and the overall effective voltage inside the NIR PeLEDs is zero, the maximum capacitance in the *C–V* characteristic appears. The decrease in capacitance as methylamine content in P3CT increases indicates that fewer carriers accumulated in the device and more carriers recombined at the emitting material layer [58].

The complex-z diagram is widely used in organic electronic devices to analyze *RC* components with equivalent circuits [59, 60]. Figures 6b,c show the complex-z plots of NIR PeLEDs devices with different MA doping HTL. It is easy to see that as the MA doping amount of the P3CT HTL increases, the size of the semi-circle in our devices' complex-z plot shrinks. When we applied a bias voltage, we obtained maximum Z′ and Z″ values of 5359 and 1945 Ω, 1139 and 501 Ω, 881 and 351Ω, 755 and 319 Ω for NIR PeLEDs with different MA doped P3CT HTL as control, 1MA, 2MA, and 3MA, respectively. The minimum Z′ value in the complex-z plot denotes the contact resistance at the electrode, which is shown as a series resistance (R_s) in the equivalent circuit. The sum of the series and parallel resistances in a parallel *RC* circuit corresponds to the maximum Z′ value. The reduced sum of parallel resistances caused by MA doping in the P3CT hole transport layer, which improves perovskite film crystal quality and thus reduces interfacial defects. For more advanced interpretations of complex-z plots, the equivalent circuit of the interfacial

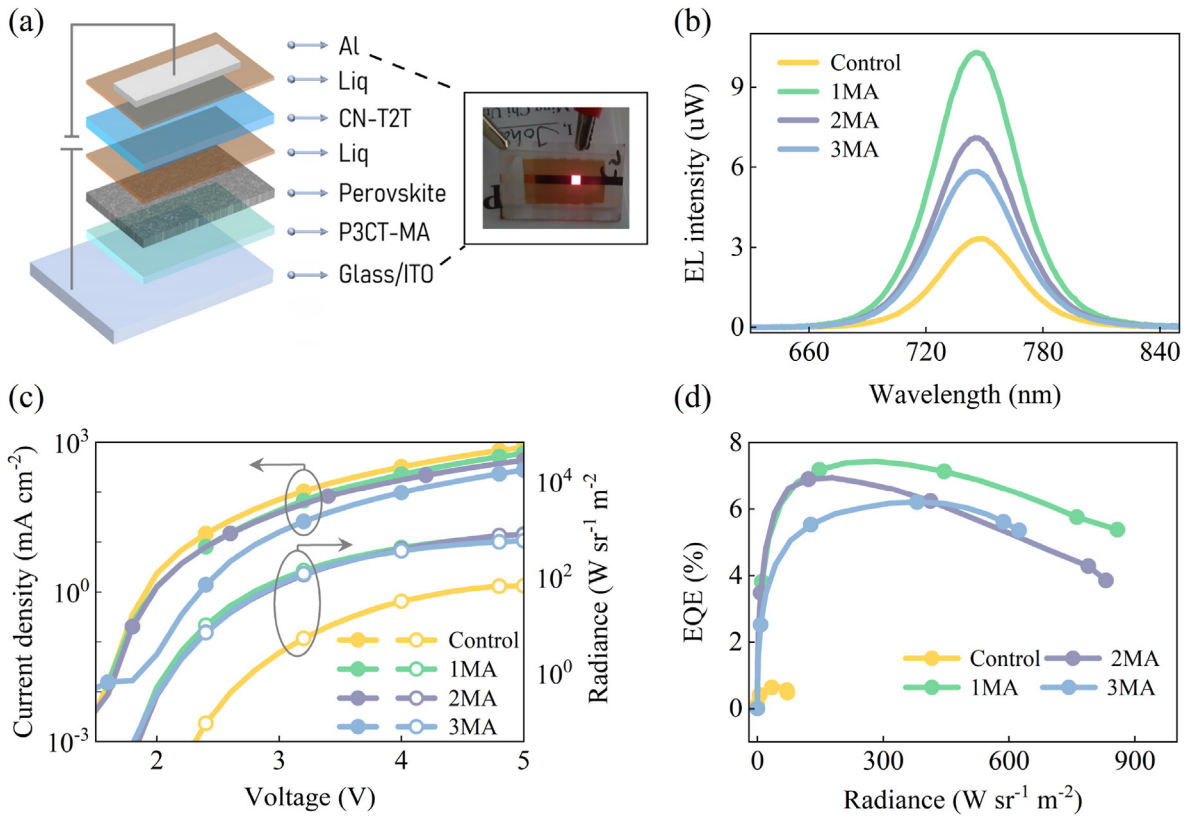

Figure 5. The performance of NIR PeLEDs with different MA ratios (a) Device structure of NIR PeLEDs, along with the respective photograph of an operating device, (b) Electroluminescence spectra, (c) Voltage – current density – radiance plots, and (d) External quantum efficiency.

Table 1. Summary of device performance based on different HTLs.

P3CT-MA HTLs	PL/EL peaks (nm)	Max. Radiance (W sr^{-1} m^{-2})	$EQE_{max/avg}$ (%)	Turn-on voltage (V)
Control	761/749	71.38	0.66/0.42	2.32
1MA	760/746	858.37	7.44/6.59	1.82
2MA	760/746	831.03	6.95/5.50	1.84
3MA	760/745	623.58	6.21/4.81	1.83

devices can be represented as two parallel *RC* circuits connected in series, plus an additional contact resistance (R_s) that defines the contact resistance between the semiconductor and the metal or conductive glasses used [61]. Two parallel RC circuits are used to simulate two distinct electrical transport phenomena within organic electronic devices [60]. The resistance and capacitance of the hole transporting layer are represented by one parallel *RC* (R_1, C_1) circuit, and the electron conducting layer is represented by the other parallel *RC* (R_2, C_2). At lower frequencies, the NIR PeLEDs with low-MA-doped P3CT HTL exhibits inductive responses (or negative capacitance), as shown in Figure 6b. As a result, an inductance (L) must be added to one parallel *RC* component of the equivalent circuit. In contrast, as shown in Figure 6c, the NIR PeLEDs with P3CT HTL and a doping molar ratio of MA greater than one requires only two parallel RC circuits. Table 2 lists the fitting parameters of the equivalent circuits for each device of different MA doping HTL. The interface resistance is significantly reduced when a higher proportion of MA doped P3CT HTL is introduced, but the interface capacitance does not change significantly. This is due to the fact that the regular arrangement of P3CT promotes crystallization and bonding strength of the interfacial perovskite grains on the P3CT layers. Although the excess MA facilitates the collection of holes while exciton dissociation occurs at the interface, which improves the efficiency of solar cells or photodetectors, for light-emitting diodes, it will eventually cause holes to be difficult to transport from the HTL to the EML, reducing the number of

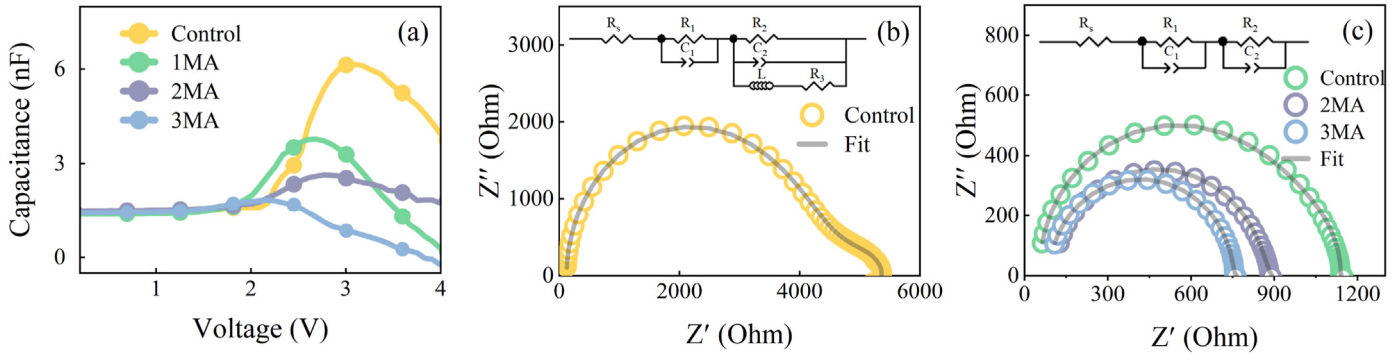

Figure 6. (a) Capacitance–Voltage (C–V) curve of perovskite LEDs with different HTLs, (b) and (c) Nyquist plot of perovskite LEDs with different HTLs along with equivalent circuit (inset).

Table 2. EIS parameters obtained by fitting the Nyquist plots with the equivalent circuit for the perovskite LED based on different HTLs.

Devices	R_s (Ω) (%)	R_1 (Ω) (%)	C_1 (nF) (%)	R_2 (Ω) (%)	C_2 (nF) (%)	L (H) (%)	R_3 (Ω) (%)
Control	107.2 ± 0.95	3925 ± 0.22	2.35 ± 0.29	1745 ± 1.71	2283.2 ± 2.34	0.29 ± 8.26	5998 ± 5.93
1MA	64.6 ± 0.94	715 ± 0.23	0.94 ± 0.31	370.8 ± 0.63	26.1 ± 0.97		
2MA	113.1 ± 0.37	435 ± 0.22	0.96 ± 0.33	334.7 ± 0.33	20.1 ± 0.58		
3MA	95.6 ± 0.33	304 ± 0.26	1.01 ± 0.35	363.8 ± 0.36	8.87 ± 0.51		

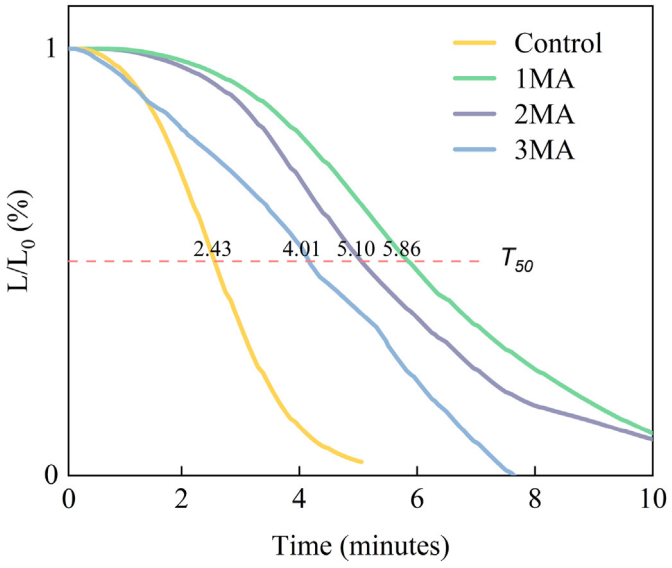

Figure 7. Operational stability of NIR PeLEDs with encapsulation measured under ambient conditions as a function of operation time at a constant current density of 10 mA cm^{-2}.

electron-hole recombination and the *EQE*. The phenomenon of a lower frequency inductive response for the NIR PeLEDs with low-MA-doped P3CT HTL is similar to previous studies of OLED systems under bipolar injection conditions, where recombination occurs via localized trap states [62, 63]. This is consistent with carrier traps caused by grain boundary defects or volume defects caused by the perovskite layer's imperfect crystal structure due to the low MA doped HTL. Due to the better crystalline structure of perovskite EML, no inductive response occurs in perovskite LEDs with higher MA doping. The NIR PeLEDs with the 1MA doped P3CT HTL has the lowest contact resistance (R_s), which smoothest carrier injection in the perovskite layers on both electrodes, resulting in better NIR PeLEDs performance.

Unbalanced carrier injection in LEDs can significantly reduce performance and shorten the device's lifetime. Charging is the main cause of device degradation in NIR PeLEDs, and suppressing charging is expected to improve device stability [64]. Based on this hypothesis, we tested the device's stability to investigate the effect of balanced charge transfer in the device. The time for the EL intensity to decay to 50% of its maximum value, T_{50}, of an encapsulated device under a constant current density of 10 mA cm^2 was determined to be 2.43, 5.86, 5.10, and 4.01 min for the control, 1MA, 2MA, and 3MA-based NIR PeLEDs, respectively, as shown in Figure 7.

4. Conclusions

In summary, we demonstrated that P3CT-MA with an optimal MA molar ratio can boost device performance through improved hole injection, which leads to balanced charge injection. In comparison to the control device, 1MA-based devices achieved an eleven-fold improvement in EQE and a twelve-fold improvement in device radiance. The research presented here proposes an alternative HTL for producing highly efficient NIR PeLEDs with good reproducibility.

Declarations

Author contribution statement

Chih-Chien Lee, Shun-Wei Liu: Contributed reagents, materials, analysis tools or data.

Johan Iskandar: Conceived and designed the experiments; Performed the experiments; Analyzed and interpreted the data; Wrote the paper.

Ade Kurniawan: Performed the experiments.

Hung-Pin Hsu, Ya-Fen Wu: Analyzed and interpreted the data.

Hsin-Ming Cheng: Conceived and designed the experiments; Contributed reagents, materials, analysis tools or data; Wrote the paper.

Funding statement

This work was supported by the Ministry of Science and Technology, Taiwan (MOST 110-2221-E-011-104-, MOST 110-2112-M-131-002-MY3, MOST 109-2223-E-131-001-MY3).

Data availability statement

Data will be made available on request.

Declaration of interests statement

The authors declare no conflict of interest.

Additional information

Supplementary content related to this article has been published online at https://doi.org/10.1016/j.heliyon.2022.e10504.

References

[1] R. Dong, Y. Fang, J. Chae, J. Dai, Z. Xiao, Q. Dong, Y. Yuan, A. Centrone, X.C. Zeng, J. Huang, High-gain and low-driving-voltage photodetectors based on organolead triiodide perovskites, Adv. Mater. 27 (2015) 1912–1918.

[2] A. Swarnkar, A.R. Marshall, E.M. Sanehira, B.D. Chernomordik, D.T. Moore, J.A. Christians, T. Chakrabarti, J.M. Luther, Quantum dot-induced phase stabilization of α-CsPbI3 perovskite for high-efficiency photovoltaics, Science (80-.) 354 (2016) 92–95.

[3] B. Yang, F. Zhang, J. Chen, S. Yang, X. Xia, T. Pullerits, W. Deng, K. Han, Ultrasensitive and fast all-inorganic perovskite-based photodetector via fast carrier diffusion, Adv. Mater. 29 (2017) 1–8.

[4] P.A. Jaeki Jeong, Minjin Kim, Jongdeuk Seo, Haizhou Lu, M.K. Aditya Mishra, Yingguo Yang, Michael A. Hope, Felix T. Eickemeyer, Y.J. Yung Jin Yoon, In Woo Choi, Barbara Primera Darwich, Seung Ju Choi, U.R. Jun Hee Lee, Bright Walker, Shaik M. Zakeeruddin, M.G. Lyndon Emsley, J.Y.K. Anders Hagfeldt, Dong Suk Kim, Pseudo-halide anion engineering for α-FAPbI3 perovskite solar cells, Nature 592 (2020) 381–385.

[5] H. Min, D.Y. Lee, J. Kim, G. Kim, K.S. Lee, J. Kim, M.J. Paik, Y.K. Kim, K.S. Kim, M.G. Kim, T.J. Shin, S. Il Seok, Perovskite solar cells with atomically coherent interlayers on SnO2 electrodes, Nature 598 (2021) 444–450.

[6] H. Huang, A.S. Susha, S.V. Kershaw, T.F. Hung, A.L. Rogach, Control of emission color of high quantum yield CH3NH3PbBr3 perovskite quantum dots by Precipitation temperature, Adv. Sci. 2 (2015) 1–5.

[7] L. Protesescu, S. Yakunin, M.I. Bodnarchuk, F. Krieg, R. Caputo, C.H. Hendon, R.X. Yang, A. Walsh, M.V. Kovalenko, Nanocrystals of Cesium lead halide perovskites (CsPbX3, X = Cl, Br, and I): novel optoelectronic materials showing bright emission with wide color gamut, Nano Lett. 15 (2015) 3692–3696.

[8] Y.H. Kim, H. Cho, J.H. Heo, T.S. Kim, N.S. Myoung, C.L. Lee, S.H. Im, T.W. Lee, Multicolored organic/inorganic hybrid perovskite light-emitting diodes, Adv. Mater. 27 (2015) 1248–1254.

[9] G. Li, F.W.R. Rivarola, N.J.L.K. Davis, S. Bai, T.C. Jellicoe, F. De La Peña, S. Hou, C. Ducati, F. Gao, R.H. Friend, N.C. Greenham, Z.K. Tan, Highly efficient perovskite nanocrystal light-emitting diodes enabled by a universal Crosslinking method, Adv. Mater. 28 (2016) 3528–3534.

[10] N. Wang, L. Cheng, R. Ge, S. Zhang, Y. Miao, W. Zou, C. Yi, Y. Sun, Y. Cao, R. Yang, Y. Wei, Q. Guo, Y. Ke, M. Yu, Y. Jin, Y. Liu, Q. Ding, D. Di, L. Yang, G. Xing, H. Tian, C. Jin, F. Gao, R.H. Friend, J. Wang, W. Huang, Perovskite light-emitting diodes based on solution-processed self-organized multiple quantum wells, Nat. Photonics 10 (2016) 699–704.

[11] J. Si, Y. Liu, Z. He, H. Du, K. Du, D. Chen, J. Li, M. Xu, H. Tian, H. He, D. Di, C. Lin, Y. Cheng, J. Wang, Y. Jin, Efficient and high-color-purity light-emitting diodes based on in Situ grown films of CsPbX3 (X = Br, I) nanoplates with controlled thicknesses, ACS Nano 11 (2017) 11100–11107.

[12] X. Yang, X. Zhang, J. Deng, Z. Chu, Q. Jiang, J. Meng, P. Wang, L. Zhang, Z. Yin, J. You, Efficient green light-emitting diodes based on quasi-two-dimensional composition and phase engineered perovskite with surface passivation, Nat. Commun. 9 (2018) 2–9.

[13] Z. Xiao, R.A. Kerner, N. Tran, L. Zhao, G.D. Scholes, B.P. Rand, Engineering perovskite nanocrystal surface termination for light-emitting diodes with external quantum efficiency exceeding 15, Adv. Funct. Mater. 29 (2019) 1–7.

[14] L. Zhao, K. Roh, S. Kacmoli, K. Al Kurdi, S. Jhulki, S. Barlow, S.R. Marder, C. Gmachl, B.P. Rand, Thermal management enables bright and stable perovskite light-emitting diodes, Adv. Mater. 32 (2020) 1–7.

[15] Y.F. Liu, Y.F. Zhang, M. Xu, Z.Y. Zhang, J. Tao, Y. Gu, J. Feng, H.B. Sun, Enhanced performance of perovskite light-emitting devices with improved perovskite crystallization, IEEE Photonics J 9 (2017).

[16] V. Prakasam, F. Di Giacomo, R. Abbel, D. Tordera, M. Sessolo, G. Gelinck, H.J. Bolink, Efficient perovskite light-emitting diodes: effect of composition, morphology, and transport layers, ACS Appl. Mater. Interfaces 10 (2018) 41586–41591.

[17] Y. Miao, Y. Ke, N. Wang, W. Zou, M. Xu, Y. Cao, Y. Sun, R. Yang, Y. Wang, Y. Tong, W. Xu, L. Zhang, R. Li, J. Li, H. He, Y. Jin, F. Gao, W. Huang, J. Wang, Stable and bright formamidinium-based perovskite light-emitting diodes with high energy conversion efficiency, Nat. Commun. 10 (2019) 1–7.

[18] H. Zhang, C. Tu, C. Xue, J. Wu, Y. Cao, W. Zou, W. Xu, K. Wen, J. Zhang, Y. Chen, J. Lai, L. Zhu, K. Pan, L. Xu, Y. Wei, H. Lin, N. Wang, W. Huang, J. Wang, Low roll-off and high stable electroluminescence in three-dimensional FAPbI3Perovskites with Bifunctional-molecule additives, Nano Lett. 21 (2021) 3738–3744.

[19] C.C. Lee, J. Iskandar, A.K. Akbar, H.M. Cheng, S.W. Liu, Controllable crystallization based on the aromatic ammonium additive for efficiently near-infrared perovskite light-emitting diodes, Org. Electron. 99 (2021), 106327.

[20] T. Dittrich, F. Lang, O. Shargaieva, J. Rappich, N.H. Nickel, E. Unger, B. Rech, Diffusion length of photo-generated charge carriers in layers and powders of CH3NH3PbI3 perovskite, Appl. Phys. Lett. 109 (2016) 1–5.

[21] H. Lin, L. Zhu, H. Huang, C.J. Reckmeier, C. Liang, A.L. Rogach, W.C.H. Choy, Efficient near-infrared light-emitting diodes based on organometallic halide perovskite-poly(2-ethyl-2-oxazoline) nanocomposite thin films, Nanoscale 8 (2016) 19846.

[22] H. Cho, S.H. Jeong, M.H. Park, Y.H. Kim, C. Wolf, C.L. Lee, J.H. Heo, A. Sadhanala, N.S. Myoung, S. Yoo, S.H. Im, R.H. Friend, T.W. Lee, Overcoming the electroluminescence efficiency limitations of perovskite light-emitting diodes, Science (80-.) 350 (2015) 1222–1225.

[23] Z. Xiao, R.A. Kerner, L. Zhao, N.L. Tran, K.M. Lee, T.W. Koh, G.D. Scholes, B.P. Rand, Efficient perovskite light-emitting diodes featuring nanometre-sized crystallites, Nat. Photonics 11 (2017) 108–115.

[24] S. Wieghold, J.P. Correa-Baena, L. Nienhaus, S. Sun, K.E. Shulenberger, Z. Liu, J.S. Tresback, S.S. Shin, M.G. Bawendi, T. Buonassisi, Precursor concentration affects grain size, crystal orientation, and local performance in mixed-ion lead perovskite solar cells, ACS Appl. Energy Mater. 1 (2018) 6801–6808.

[25] M. You, H. Wang, F. Cao, C. Zhang, T. Zhang, L. Kong, L. Wang, D. Zhao, J. Zhang, X. Yang, Improving efficiency and stability in quasi-2D perovskite light-emitting diodes by a multifunctional LiF interlayer, ACS Appl. Mater. Interfaces 12 (2020) 43018–43023.

[26] Y. Lu, Z. Wang, J. Chen, Y. Peng, X. Tang, Z. Liang, F. Qi, W. Chen, Tuning hole transport layers and optimizing perovskite films thickness for high efficiency CsPbBr3 nanocrystals electroluminescence light-emitting diodes, J. Lumin. 234 (2021), 117952.

[27] X. Li, X. Liu, X. Wang, L. Zhao, T. Jiu, J. Fang, Polyelectrolyte based hole-transporting materials for high performance solution processed planar perovskite solar cells, J. Mater. Chem. A. 3 (2015) 15024–15029.

[28] X. Li, Y.C. Wang, L. Zhu, W. Zhang, H.Q. Wang, J. Fang, Improving efficiency and reproducibility of perovskite solar cells through aggregation control in polyelectrolytes hole transport layer, ACS Appl. Mater. Interfaces 9 (2017) 31357–31361.

[29] S. Li, Y.L. Cao, W.H. Li, Z.S. Bo, A brief review of hole transporting materials commonly used in perovskite solar cells, Rare Met. 40 (2021) 2712–2729.

[30] Y.H. Kim, C. Wolf, H. Kim, T.W. Lee, Charge carrier recombination and ion migration in metal-halide perovskite nanoparticle films for efficient light-emitting diodes, Nano Energy 52 (2018) 329–335.

[31] L.M. Herz, Charge-carrier mobilities in metal halide perovskites: fundamental mechanisms and limits, ACS Energy Lett. 2 (2017) 1539–1548.

[32] H. Fan, F. Li, P. Wang, Z. Gu, J.H. Huang, K.J. Jiang, B. Guan, L.M. Yang, X. Zhou, Y.L. Song, Methylamine-assisted growth of uniaxial-oriented perovskite thin films with millimeter-sized grains, Nat. Commun. 11 (2020) 1–10.

[33] R.A. Kerner, T.H. Schloemer, P. Schulz, J.J. Berry, J. Schwartz, A. Sellinger, B.P. Rand, Amine additive reactions induced by the soft Lewis acidity of Pb2+ in halide perovskites. Part II: impacts of amido Pb impurities in methylammonium lead triiodide thin films, J. Mater. Chem. C 7 (2019) 5244–5250.

[34] Z. Zhu, Y. Bai, H.K.H. Lee, C. Mu, T. Zhang, L. Zhang, J. Wang, H. Yan, S.K. So, S. Yang, Polyfluorene derivatives are high-performance organic hole-transporting materials for inorganic-organic hybrid perovskite solar cells, Adv. Funct. Mater. 24 (2014) 7357–7365.

[35] M. Wang, W. Li, H. Wang, K. Yang, X. Hu, K. Sun, S. Lu, Z. Zang, Small molecule modulator at the interface for efficient perovskite solar cells with high short-circuit current density and Hysteresis free, Adv. Electron. Mater. 6 (2020).

[36] T. Chen, W.L. Chen, B.J. Foley, J. Lee, J.P.C. Ruff, J.Y.P. Ko, C.M. Brown, L.W. Harriger, D. Zhang, C. Park, M. Yoon, Y.M. Chang, J.J. Choi, S.H. Lee, Origin of long lifetime of band-edge charge carriers in organic–inorganic lead iodide perovskites, Proc. Natl. Acad. Sci. U. S. A 114 (2017) 7519–7524.

[37] W. Kong, Z. Ye, Z. Qi, B. Zhang, M. Wang, A. Rahimi-Iman, H. Wu, Characterization of an abnormal photoluminescence behavior upon crystal-phase transition of perovskite CH3NH3PbI3, Phys. Chem. Chem. Phys. 17 (2015) 16405–16411.

[38] B. Tang, L.J. Ruan, C. Qin, A. Shu, H. He, Y. Ma, High stability and temperature-dependent photoluminescence of orthorhombic CsPbI3 perovskite nanoparticles, Adv. Opt. Mater. 8 (2020) 1–8.

[39] Y. Liu, H. Lu, J. Niu, H. Zhang, S. Lou, C. Gao, Y. Zhan, X. Zhang, Q. Jin, L. Zheng, Temperature-dependent photoluminescence spectra and decay dynamics of MAPbBr3 and MAPbI3 thin films, AIP Adv. 8 (2018).

[40] F. Zhang, Z.F. Shi, Z.Z. Ma, Y. Li, S. Li, D. Wu, T.T. Xu, X.J. Li, C.X. Shan, G.T. Du, Silica coating enhances the stability of inorganic perovskite nanocrystals for efficient and stable down-conversion in white light-emitting devices, Nanoscale 10 (2018) 20131–20139.

[41] Y.P. Varshni, Temperature dependence of the energy gap in semiconductors, Physica 34 (1967) 149–154.

[42] B.T. Diroll, H. Zhou, R.D. Schaller, Low-temperature absorption, photoluminescence, and lifetime of CsPbX3 (X = Cl, Br, I) nanocrystals, Adv. Funct. Mater. 28 (2018) 1–7.

[43] K.P. Goetz, A.D. Taylor, F. Paulus, Y. Vaynzof, Shining light on the photoluminescence properties of metal halide perovskites, Adv. Funct. Mater. 30 (2020).

[44] M. Baranowski, P. Plochocka, Excitons in metal-halide perovskites, Adv. Energy Mater. 10 (2020).

[45] M. Yu, S. Yuan, H.Y. Wang, J.S. Zhao, Y. Qin, L.M. Fu, J.P. Zhang, X.C. Ai, Characterization of the influences of morphology on the intrinsic properties of perovskite films by temperature-dependent and time-resolved spectroscopies, Phys. Chem. Chem. Phys. 20 (2018) 6575–6581.

[46] S. Kalytchuk, O. Zhovtiuk, S.V. Kershaw, R. Zbořil, A.L. Rogach, Temperature-dependent exciton and trap-related photoluminescence of CdTe quantum dots embedded in a NaCl matrix: implication in thermometry, Small 12 (2016) 466–476.

[47] R. Chen, Q.L. Ye, T. He, V.D. Ta, Y. Ying, Y.Y. Tay, T. Wu, H. Sun, Exciton localization and optical properties improvement in nanocrystal-embedded ZnO core-shell nanowires, Nano Lett. 13 (2013) 734–739.

[48] W. Kong, A. Rahimi-Iman, G. Bi, X. Dai, H. Wu, Oxygen intercalation induced by Photocatalysis on the surface of hybrid lead halide perovskites, J. Phys. Chem. C 120 (2016) 7606–7611.

[49] A. Mishra, Z. Ahmad, F. Touati, R.A. Shakoor, M.K. Nazeeruddin, One-dimensional facile growth of MAPbI3 perovskite micro-rods, RSC Adv. 9 (2019) 11589–11594.

[50] Z. Liang, S. Zhang, X. Xu, N. Wang, J. Wang, X. Wang, Z. Bi, G. Xu, N. Yuan, J. Ding, A large grain size perovskite thin film with a dense structure for planar heterojunction solar cells via spray deposition under ambient conditions, RSC Adv. 5 (2015) 60562–60569.

[51] H. Wang, X. Gong, D. Zhao, Y.B. Zhao, S. Wang, J. Zhang, L. Kong, B. Wei, R. Quintero-Bermudez, O. Voznyy, Y. Shang, Z. Ning, Y. Yan, E.H. Sargent, X. Yang, A multi-functional molecular modifier enabling efficient large-area perovskite light-emitting diodes, Joule 4 (2020) 1977–1987.

[52] Z. Wen, F. Xie, W.C.H. Choy, Stability of electroluminescent perovskite quantum dots light-emitting diode, Nano Sel. (2021) 1–26.

[53] G. Lozano, The role of metal halide perovskites in next-generation lighting devices, J. Phys. Chem. Lett. 9 (2018) 3987–3997.

[54] Y. Cheng, H.W. Li, J. Zhang, Q.D. Yang, T. Liu, Z. Guan, J. Qing, C.S. Lee, S.W. Tsang, Spectroscopic study on the impact of methylammonium iodide loading time on the electronic properties in perovskite thin films, J. Mater. Chem. A. 4 (2015) 561–567.

[55] X. Sun, C. Han, K. Wang, H. Yu, J. Li, K. Lu, J. Qin, H. Yang, L. Deng, F. Zhao, Q. Yang, B. Hu, Effect of Bathocuproine organic additive on optoelectronic properties of highly efficient methylammonium lead Bromide perovskite light-emitting diodes, ACS Appl. Energy Mater. 1 (2018) 6992–6998.

[56] H. Kim, L. Zhao, J.S. Price, A.J. Grede, K. Roh, A.N. Brigeman, M. Lopez, B.P. Rand, N.C. Giebink, Hybrid perovskite light emitting diodes under intense electrical excitation, Nat. Commun. 9 (2018).

[57] F.-W. Yang, Y.-S. You, S.-W. Feng, Efficient carrier injection, transport, relaxation, and recombination associated with a stronger carrier localization and a low Polarization effect of nonpolar mplane inGaN/GaN light-emitting diodes, Nanoscale 12 (2017).

[58] H. Lee, B.G. Jeong, W.K. Bae, D.C. Lee, J. Lim, Surface state-induced barrierless carrier injection in quantum dot electroluminescent devices, Nat. Commun. 12 (2021) 1–9.
[59] S.H. Kim, K.H. Choi, H.M. Lee, D.H. Hwang, L.M. Do, H.Y. Chu, T. Zyung, Impedance spectroscopy of single- and double-layer polymer light-emitting diode, J. Appl. Phys. 87 (2000) 882–888.
[60] C.C. Chen, B.C. Huang, M.S. Lin, Y.J. Lu, T.Y. Cho, C.H. Chang, K.C. Tien, S.H. Liu, T.H. Ke, C.C. Wu, Impedance spectroscopy and equivalent circuits of conductively doped organic hole-transport materials, Org. Electron. 11 (2010) 1901–1908.
[61] S.M. Han, K.P. Kim, D.C. Choo, T.W. Kim, J.H. Seo, Y.K. Kim, Equivalent circuit models in organic light-emitting diodes designed using a cole-cole plot, Mol. Cryst. Liq. Cryst. 470 (2007) 279–287.
[62] E. Ehrenfreund, C. Lungenschmied, G. Dennler, H. Neugebauer, N.S. Sariciftci, Negative capacitance in organic semiconductor devices: bipolar injection and charge recombination mechanism, Appl. Phys. Lett. 91 (2007) 1–4.
[63] S. Nowy, W. Ren, A. Elschner, W. Lövenich, W. Brütting, Impedance spectroscopy as a probe for the degradation of organic light-emitting diodes, J. Appl. Phys. 107 (2010) 1–10.
[64] J.H. Chang, P. Park, H. Jung, B.G. Jeong, D. Hahm, G. Nagamine, J. Ko, J. Cho, L.A. Padilha, D.C. Lee, C. Lee, K. Char, W.K. Bae, Unraveling the origin of operational instability of quantum dot based light-emitting diodes, ACS Nano 12 (2018) 10231–10239.